Eur. Phys. J. C (2009) 60: 233–247
DOI 10.1140/epjc/s10052-009-0868-7

THE EUROPEAN PHYSICAL JOURNAL C

Regular Article - Theoretical Physics

Elastic and quasi-elastic pp and $\gamma^\star p$ scattering in the dipole model*

Christoffer Flensburg[1,a], **Gösta Gustafson**[1,2,b], **Leif Lönnblad**[1,c]

[1]Dept. of Theoretical Physics, Lund University, Sölvegatan 14A, 223 62 Lund, Sweden
[2]II. Institut für Theoretische Physik, Universität Hamburg, Luruper Chaussee 149, 22761 Hamburg, Germany

Received: 14 July 2008 / Revised: 5 November 2008 / Published online: 12 February 2009

Abstract We have in earlier papers presented an extension of Mueller's dipole cascade model, which includes subleading effects from energy conservation and running coupling as well as color-suppressed saturation effects from pomeron loops via a "dipole swing". The model was applied to the description of the total and diffractive cross sections in pp and $\gamma^* p$ collisions, and also the elastic cross section in pp scattering. In this paper we extend the model to the description of the corresponding quasi-elastic cross sections in $\gamma^* p$, namely the exclusive production of vector mesons and deeply virtual Compton scattering. Also for these reactions we find good agreement with measured cross sections. In addition, we obtain a reasonable description of the t-dependence of the elastic pp and quasi-elastic $\gamma^\star p$ cross sections.

1 Introduction

We have in a series of papers [1–3] presented an extension of Mueller's dipole cascade model [4–6] implemented in a Monte Carlo program, which includes sub-leading effects from energy conservation and running coupling, as well as color-suppressed effects from pomeron loops via a *dipole swing* mechanism. It also includes a consistent treatment of non-perturbative confinement effects, which suppress dipoles with large transverse extension.

The advantage of a cascade model formulated in transverse coordinate space is the possibility to include effects of multiple collisions and saturation in a straightforward way. While analytic results have mainly been presented for the asymptotic behavior of total and diffractive cross sections, Monte Carlo simulations facilitate studies of non-leading effects and more quantitative results. A simulation of Mueller's initial model was presented by Salam in [7]. Although giving finite results for the total cross section, this leading-log evolution suffers from divergences for small dipoles, which caused numerical problems with very large gluon multiplicities and prevented simulations at higher energies. One important result from this analysis was the very large fluctuations in the evolution [8]. As the ratio between the elastic and the total cross sections is determined by fluctuations in the scattering process, this implies that less fluctuations are needed in the impact-parameter dependence, to reproduce the experimental data. As a result we found in [3] that including the fluctuations in the evolution implies that the impact-parameter profile is not as "black and white" as in analyses in which only fluctuations in the impact parameter are taken into account.

In the model described in [1–3] we include a number of sub-leading effects, with the aim that we in the end will be able to describe not only the total and diffractive cross sections, but also to generate fully exclusive final states. The main ingredient in our model is energy conservation, which is included by assigning a transverse momentum to each emitted gluon given by the maximum inverse size of the neighboring dipoles. As a result this also implies that the singularities for small dipoles are avoided. Other features are saturation effects in the evolution through a dipole swing mechanism, and a consistent treatment of confinement and running-coupling effects in both dipole emissions and dipole–dipole interactions.

Taken together with a very simple model for the initial proton wave function, these features allow us to obtain a Lorentz-frame independent description of total cross sections, both for pp and DIS, using basically only two free

*Work supported in part by the Marie Curie RTN "MCnet" (contract number MRTN-CT-2006-035606), by the Swedish Foundation for International Cooperation and Higher Education–STINT (contract number 2006/080) and by the Deutsche Forschungsgemeinschaft.

[a] e-mail: christoffer.flensburg@thep.lu.se
[b] e-mail: gosta.gustafson@thep.lu.se
[c] e-mail: leif.lonnblad@thep.lu.se

parameters, a confinement scale $r_{\max}$ and $\Lambda_{\rm QCD}$ [3]. The model gives a good description of measurements of the total and diffractive cross sections in pp and $\gamma^* p$ collisions, and also of the elastic cross section in pp. In this paper we will continue our investigations with an analysis of exclusive production of vector mesons and real photons in $\gamma^* p$. The aim is to further test our model, and in particular to study the effect of the fluctuations in the cascade. We also extend the analyses to include the t-dependence of the (quasi-) elastic cross sections, including also elastic pp scattering, which in particular gives information about the properties of the incoming proton state. We here include the effects of scewedness in the photon wave function, but we argue that such effects in the proton wave function ought to be small at HERA and proton collider energies.

In the eikonal approximation the quasi-elastic $\gamma^* p$ collisions contain three elements: the virtual photon–dipole vertex, the dipole–proton scattering amplitude, and the vertex for the transition between the dipole and the final vector meson or real photon. Here the first component can be calculated perturbatively, although a hadronic component must be included at lower Q^2-values. In an extensive study Forshaw et al. [9, 10] have analyzed the results obtained from a set of models for the dipole–proton scattering and for the vector meson wave functions, and compared them with experimental data. In this paper we want to carry out a similar analysis, but we now use our dipole cascade model for the dipole–proton scattering. We are here particularly interested in the effects of fluctuations in the cascade evolution, which are not included in the analyses by Forshaw et al. We also want to use this study to put constraints on the state of the incoming proton.

An approach to describe both pp and $\gamma^* p$ collisions in a dipole formalism has also been presented by Shoshi et al. [11]. One essential difference is that in their approach the energy dependence is described by a combination of a soft and a hard pomeron, with parameters fit to the data. In our model the energy dependence is fully determined by the perturbative dipole cascade evolution. Naturally this dynamical description limits the application of our model to relatively high energies.

We begin in Sect. 2 with discussing the eikonal formalism for exclusive vector meson production, whereafter we describe our model for dipole evolution and dipole–dipole scattering in Sect. 3 and the models we use for the proton, photon and vector meson wave functions in Sect. 4. In Sect. 5 we retune the parameters of our model to the data on total and elastic pp cross sections and the total $\gamma^\star p$ cross section before we present our results on quasi-elastic $\gamma^\star p$ cross sections in Sect. 6. Finally, we present our conclusions in Sect. 7

2 Formalism

2.1 The dipole cascade model and the eikonal approximation

As discussed in the introduction, our model for pp collisions and DIS is an extension of Mueller's dipole cascade model [4–6]. In this formalism the probability per unit rapidity Y that a dipole $(\mathbf{x}, \mathbf{y})$ emits a gluon at transverse position $\mathbf{z}$ is given by

$$\frac{\mathrm{d}\mathcal{P}}{\mathrm{d}Y} = \frac{\bar{\alpha}}{2\pi}\,\mathrm{d}^2\mathbf{z}\frac{(\mathbf{x}-\mathbf{y})^2}{(\mathbf{x}-\mathbf{z})^2(\mathbf{z}-\mathbf{y})^2}, \quad \text{with } \bar{\alpha} = \frac{3\alpha_{\rm s}}{\pi}. \tag{2.1}$$

The evolution of this cascade agrees with the leading-order BFKL evolution. As a consequence, the total number of dipoles grows exponentially. This also implies a strong growth for the total cross section, which, however, is tamed by taking multiple dipole interactions into account. The scattering probability between two elementary color dipoles with coordinates $(\mathbf{x}_i, \mathbf{y}_i)$ and $(\mathbf{x}_j, \mathbf{y}_j)$, respectively, is given by

$$\begin{aligned} f_{ij} &= f(\mathbf{x}_i, \mathbf{y}_i | \mathbf{x}_j, \mathbf{y}_j) \\ &= \frac{\alpha_{\rm s}^2}{8}\left[\log\left(\frac{(\mathbf{x}_i-\mathbf{y}_j)^2(\mathbf{y}_i-\mathbf{x}_j)^2}{(\mathbf{x}_i-\mathbf{x}_j)^2(\mathbf{y}_i-\mathbf{y}_j)^2}\right)\right]^2. \end{aligned} \tag{2.2}$$

Within this eikonal formalism the transverse coordinates are not changed under the emission or scattering processes in (2.1) and (2.2). Therefore, unitarity constraints and multiple scattering are easily accounted for by the exponentiated expression

$$T(\mathbf{b}) = 1 - \mathrm{e}^{-\sum f_{ij}} \equiv 1 - \mathrm{e}^{-F}, \tag{2.3}$$

which implies that the scattering probability never exceeds 1. We note that the splitting probability in (2.1) is singular for small dipole sizes $\mathbf{x}-\mathbf{z}$ or $\mathbf{z}-\mathbf{y}$, but these small dipoles have a small probability to interact with the target, and the eikonal $F = \sum f_{ij}$ is finite.

In the model developed in [1–3], we extended Mueller's cascade model to include sub-leading effects from energy conservation and a running coupling, saturation effects not only in the dipole–dipole subcollisions but also within the individual cascades, and effects of confinement. These features are further discussed in Sect. 3.

The model is supplemented by a non-perturbative model for an initial proton in terms of three dipoles. In the eikonal approximation the total and the diffractive (including the elastic) cross sections are then given by

$$\begin{aligned} \sigma_{\rm tot} &= 2\int \mathrm{d}^2 b \left\langle \left(1 - \mathrm{e}^{-F}\right)\right\rangle, \\ \sigma_{\rm diff} &= \int \mathrm{d}^2 b \left\langle \left(1 - \mathrm{e}^{-F}\right)^2\right\rangle. \end{aligned} \tag{2.4}$$

The diffractive cross section can be separated in elastic scattering and diffractive excitation:

$$\sigma_{\rm el} = \int \mathrm{d}^2b \big(\langle 1 - \mathrm{e}^{-F}\rangle\big)^2,$$
$$\sigma_{\rm diff\,exc} = \int \mathrm{d}^2b \big\{\big\langle \big(1 - \mathrm{e}^{-F}\big)^2\big\rangle - \big(\langle 1 - \mathrm{e}^{-F}\rangle\big)^2\big\}. \tag{2.5}$$

Thus, the separation between elastic and inelastic diffraction is determined by the fluctuations in the scattering amplitude. The average in (2.4) and (2.5) is taken over the different incoming dipole configurations and different cascade evolutions, which thus give two separate sources for fluctuations.

2.2 DVCS and exclusive vector meson production in $\gamma^* p$ collisions

We want to study the exclusive processes

$$\gamma^* p \to V p, \quad V = \gamma, \rho, \psi, \ldots. \tag{2.6}$$

In the dipole model the virtual photon is split into a $q\bar{q}$ pair long before the collision. This dipole scatters elastically against the proton, and after the scattering the pair joins again forming a real photon or a vector meson. The formulation in the transverse coordinate plane makes it easier to study these pseudo-elastic reactions, and in the eikonal approximation the scattering amplitude is expressed in terms of three components:

$$\Im A_\lambda(s, \mathbf{b}) = s \sum_{f,h,\bar{h}} \int\int \mathrm{d}z\, \mathrm{d}^2\mathbf{r} \Psi^{*V\lambda}_{f h\bar{h}}(\mathbf{r}, z)\, \Psi^{\gamma\lambda}_{f h\bar{h}}\big(\mathbf{r}, z, Q^2\big) \times \hat{\sigma}_{\rm dp}(s, \mathbf{r}, \mathbf{b}, z). \tag{2.7}$$

Here $\mathbf{r}$ is the transverse size of the dipole, z and $1-z$ are the fractions of the photon or vector meson carried by the quark and antiquark, respectively, and h and $\bar{h}$ are their helicities. λ denotes the photon or vector meson helicity, $\hat{\sigma}_{\rm dp}$ is the dipole–proton scattering probability with $\mathbf{b}$ the impact parameter, and s the total energy squared.

Neglecting the small contribution from the real part of the amplitude, the total cross section is given by

$$\sigma_\lambda(\gamma^* p \to V p) = \frac{1}{4s^2} \int \mathrm{d}^2\mathbf{b} \big|A_\lambda(s, \mathbf{b})\big|^2. \tag{2.8}$$

2.3 Differential cross sections

For scattering of a point particle the differential cross section $\mathrm{d}\sigma_{\rm el}/\mathrm{d}t$ is obtained from the Fourier transform of the scattering amplitude in (2.3):

$$\frac{\mathrm{d}\sigma_\lambda}{\mathrm{d}t} = \frac{1}{4\pi} \left| \int \mathrm{d}^2\mathbf{b}\, \mathrm{e}^{\mathrm{i}\mathbf{q}\mathbf{b}} \langle 1 - \mathrm{e}^{-F}\rangle \right|^2, \tag{2.9}$$

with $t = -\mathbf{q}^2$. For a $q\bar{q}$ dipole described by an extended wave function $\Psi(\mathbf{r}, z)$, Bartels, Golec-Biernat and Peters [12] have shown that the effect of non-forward amplitudes (also referred to as scewedness) are properly taken into account by replacing the exponential $\mathrm{e}^{\mathrm{i}\mathbf{q}\mathbf{b}}$ by $\mathrm{e}^{\mathrm{i}\mathbf{q}(\mathbf{b}-(1-z)\mathbf{r})}$. Thus we obtain the following expression for the differential cross sections:

$$\frac{\mathrm{d}\sigma_\lambda}{\mathrm{d}t} = \frac{1}{16\pi} \left| \sum_{f,h,\bar{h}} \int\int\int \mathrm{d}z\, \mathrm{d}^2\mathbf{r}\, \mathrm{d}^2\mathbf{b}\, \mathrm{e}^{\mathrm{i}\mathbf{q}(\mathbf{b}-(1-z)\mathbf{r})} \times \Psi^{*V\lambda}_{f h\bar{h}}(\mathbf{r}, z)\, \Psi^{\gamma\lambda}_{f h\bar{h}}\big(\mathbf{r}, z, Q^2\big) \times \hat{\sigma}_{\rm dp}(s, \mathbf{r}, \mathbf{b}, z) \right|^2. \tag{2.10}$$

The effect of including the factor $\mathrm{e}^{-\mathrm{i}(1-z)\mathbf{q}\mathbf{r}}$ is small for large Q^2, where the width of the $\mathbf{r}$-distribution $\sim 1/\sqrt{z(1-z)Q^2}$ is small compared to the extension of the proton target, which in our model is determined by the parameter R_p estimated to be around 3 GeV^{-1}. As an example we find in Sect. 6 (Fig. 6.2) that for DVCS the slope of the t-distribution at $Q^2 = 8$ GeV^2 is increased by about 7%. The effect is correspondingly reduced (increased) for higher (lower) Q^2.

Naturally a similar scewedness effect should come from the dipoles within the proton. This is more difficult to estimate, but the effect should also here be determined by the ratio $((1-z)r_{\rm dipole}/R_p)^2$. In our simulations of pp collisions at the Tevatron (W = 2 TeV) we find a typical value for *those dipoles which do interact* in the collision of about 1/(1.5 GeV). (The typical size is here estimated from the median of the distribution.) Thus we estimate the effect from scewedness in the proton wave function to be of the order $((1-z)r_{\rm typical}/R_p)^2 \sim 0.01$, if typical z-values are around 0.5. A similar estimate can also be obtained from fits to minimum bias and underlying events in pp scattering. As an example, the PYTHIA event generator [13] gives a good description of the underlying events at the Tevatron if a cutoff of around 2 GeV is introduced to regularize the (mini-) jet cross section, which diverges like $dp_\perp^2/p_\perp^4$ in a collinear factorization. This cutoff value can be interpreted as a screening length which in turn can be related to a typical dipole size.

It would be valuable to study this effect in more detail to find a better quantitative estimate. However, in view of the small value of the rough estimates above, we will in the present analysis neglect the effects of scewedness in the proton wave function. We note that in the rest frame of a 2 TeV pp collision, the energy corresponds to an evolution over 7 units of rapidity for each of the protons. This corresponds to the proton evolution in DIS at $W \approx 100$ GeV, and the estimate above is therefore also relevant for the proton wave function in DIS at HERA energies.

3 The improved dipole cascade

As discussed in the introduction, the model developed in [1–3] is an extension of Mueller's dipole cascade model, which includes sub-leading effects from energy conservation and a running coupling, saturation effects not only in the dipole–dipole subcollisions but also within the individual cascades, and effects of confinement. As mentioned above, an essential point is here that we include the effect of fluctuations in the dipole cascades in the calculation of the elastic or quasi-elastic cross sections.

3.1 Non-leading perturbative effects

3.1.1 Energy-momentum conservation

It is known that the large NLO corrections to the BFKL evolution are reduced significantly if proper energy conservation is included in the leading order. In our model a small transverse extension is interpreted as a large transverse momentum. This interpretation is supported by the resulting analogies between the dipole chains in coordinate space and the chains in the LDC model, which is formulated in momentum space and interpolates smoothly between DGLAP and BFKL evolution. Taking energy-momentum conservation into account is most easily done in a Monte Carlo (MC) simulation. Conserving both light-cone components, p_+ and p_-, implies that we also satisfy the so-called consistency constraint [14]. As small dipoles in our formalism correspond to large transverse momenta, energy conservation also gives a dynamical cutoff for the otherwise diverging number of small dipoles, and thus makes the MC simulation much more efficient.

3.1.2 Running coupling

In our simulations we also include non-leading effects from the running of α_s, both in the dipole splitting and in the dipole–dipole scattering probability. In the dipole emissions the scale in the coupling is given by $\min(r, r_1, r_2)$, where r is the size of the mother dipole which splits into r_1 and r_2. This is the most natural choice and is also consistent with recent NLO calculations [15–17]. For dipole–dipole scattering the situation is somewhat more complicated with basically six different dipole sizes involved. We have chosen to use the scale $\min(|\mathbf{x}_i - \mathbf{y}_i|, |\mathbf{x}_j - \mathbf{y}_j|, |\mathbf{x}_i - \mathbf{y}_j|, |\mathbf{y}_i - \mathbf{x}_j|)$. In order to avoid divergences the coupling is in all cases frozen so that $\alpha_s(r) \to \alpha_s(\min(r, r_{\max}))$, where $r_{\max}$ is the confining scale discussed in Sect. 3.3 below.

3.2 Saturation within the cascades

Mueller's cascade includes saturation effects from multiple collisions in the Lorentz frame chosen for the calculation, but not saturation effects from gluon interaction within the individual cascades. The result is therefore dependent on the chosen Lorentz frame. In [2] we improved our model by allowing (color-suppressed) recouplings of the dipole chain during the evolution, a "dipole swing". The swing is a process in which two dipoles $(\mathbf{x}_i, \mathbf{y}_i)$ and $(\mathbf{x}_j, \mathbf{y}_j)$ are replaced by two new dipoles $(\mathbf{x}_i, \mathbf{y}_j)$ and $(\mathbf{x}_j, \mathbf{y}_i)$. The process can be interpreted in two ways. There is a probability $1/N_c^2$ that the two dipoles may have the same color, and the quark at $\mathbf{x}_i$ and the antiquark at $\mathbf{y}_j$ form a color singlet. In this case the best approximation of the quadrupole field ought to be obtained by the closest charge–anticharge combinations. Here the swing is therefore naturally suppressed by $1/N_c^2$, and it should be more likely to replace two given dipoles with two smaller ones. Secondly, we may see it as the result of a gluon exchange between the dipoles, which results in a change in the color flow. In this case the swing would be proportional to α_s^2, which again is formally suppressed by N_c^2, compared to the splitting process in (2.1), which is proportional to $\bar{\alpha} = N_c\alpha_s/\pi$.

In the MC implementation each dipole is randomly given one of N_c^2 possible color indices. Only dipoles with the same color can swing, and the weight for a swing $(\mathbf{x}_1, \mathbf{y}_1), (\mathbf{x}_2, \mathbf{y}_2) \to (\mathbf{x}_1, \mathbf{y}_2), (\mathbf{x}_2, \mathbf{y}_1)$ is determined by a factor proportional to

$$\frac{(\mathbf{x}_1 - \mathbf{y}_1)^2(\mathbf{x}_2 - \mathbf{y}_2)^2}{(\mathbf{x}_1 - \mathbf{y}_2)^2(\mathbf{x}_2 - \mathbf{y}_1)^2}. \tag{3.1}$$

This implies that the swing favors the formation of smaller dipoles. The number of dipoles is not reduced by the swing, but the fact that smaller dipoles have smaller cross sections gives the desired suppression of the total cross section. Although not explicitly frame independent, the results from the MC simulations are very nearly independent of the Lorentz frame used for the calculations.

3.3 Confinement effects

Mueller's dipole model is a purely perturbative process. It should therefore be applied to small dipoles, e.g. to heavy quarkonium states. When applying the dipole formalism to collisions with protons it is necessary to take confinement into account, in order to prevent the formation of very large dipoles. Confinement effects must also suppress long-range interactions between colliding dipoles. In [3] a consistent treatment of confinement was presented by replacing the Coulomb potentials in (2.2) and (3.3) by screened potentials, with a screening length $r_{\max}$.

Obviously the dipoles produced in the splitting process in (2.1) cannot become too large, and it is natural to introduce a scale $r_{\max}$, so that larger dipoles are suppressed. In a similar way confinement must suppress long-range interactions between colliding dipoles.

The formula for f_{ij} in (2.2) is just the two-dimensional Coulomb potential, and it can be written as

$$f(\mathbf{x}_i,\mathbf{y}_i|\mathbf{x}_j,\mathbf{y}_j) = \frac{g^4}{8}\Big[\Delta(\mathbf{x}_i-\mathbf{x}_j)-\Delta(\mathbf{x}_i-\mathbf{y}_j) - \Delta(\mathbf{y}_i-\mathbf{x}_j)+\Delta(\mathbf{y}_i-\mathbf{y}_j)\Big]^2, \tag{3.2}$$

where $\Delta(\mathbf{r})$ is the Green's function given by

$$\Delta(\mathbf{r}) = \int \frac{\mathrm{d}^2\mathbf{k}}{(2\pi)^2}\frac{\mathrm{e}^{\mathrm{i}\mathbf{k}\cdot\mathbf{r}}}{\mathbf{k}^2}. \tag{3.3}$$

To take confinement into account we replace the infinite-range Coulomb potential with a screened Yukawa potential. This implies that the Coulomb propagator $1/\mathbf{k}^2$ in (3.3) is replaced by $1/(\mathbf{k}^2+M^2)$, where $M=1/r_{\max}$ is the confinement scale. As a result, the four functions Δ in (3.2) will be replaced by

$$\int \frac{\mathrm{d}^2\mathbf{k}}{(2\pi)^2}\frac{\mathrm{e}^{\mathrm{i}\mathbf{k}\cdot\mathbf{r}}}{\mathbf{k}^2+1/r_{\max}^2} = \frac{1}{2\pi}K_0(r/r_{\max}), \tag{3.4}$$

with K_0 a modified Bessel function. For small separations, where $r \ll r_{\max}$, the function $K_0(r/r_{\max})$ behaves like $\ln(r_{\max}/r)$, and we then recognize the result in (2.2). For large separations, $r \gg r_{\max}$, $K_0(r/r_{\max})$ falls off exponentially $\sim\sqrt{\frac{\pi r_{\max}}{r}}\mathrm{e}^{-r/r_{\max}}$, as expected from confinement.

In a similar way, the underlying Coulomb potential in the dipole splitting function in (2.1) can be replaced by a screened Yukawa potential, using again the replacement $1/\mathbf{k}^2 \to 1/(\mathbf{k}^2+1/r_{\max}^2)$. The modified splitting probability is then given by

$$\frac{\mathrm{d}\mathcal{P}}{\mathrm{d}Y} \to \frac{\bar{\alpha}}{2\pi}\mathrm{d}^2\mathbf{z}\left\{\frac{1}{r_{\max}}\frac{\mathbf{x}-\mathbf{z}}{|\mathbf{x}-\mathbf{z}|}K_1\left(\frac{|\mathbf{x}-\mathbf{z}|}{r_{\max}}\right) - \frac{1}{r_{\max}}\frac{\mathbf{y}-\mathbf{z}}{|\mathbf{y}-\mathbf{z}|}K_1\left(\frac{|\mathbf{y}-\mathbf{z}|}{r_{\max}}\right)\right\}^2. \tag{3.5}$$

For small arguments, $K_1(r/r_{\max}) \approx r_{\max}/r$, we get back the result in (2.1), while for large arguments, $K_1(r/r_{\max}) \sim \sqrt{\pi r_{\max}/r}\cdot\mathrm{e}^{-r/r_{\max}}$, once again we obtain an exponentially decaying field.

4 Initial wave functions

4.1 Proton wave function

In [2] we also introduced a simple model for the proton in terms of three dipoles with extensions determined by a Gaussian distribution. The resulting model was in good agreement with total cross sections for both DIS and pp collisions. It was shown in [18] that, although a full gluon cascade from three valence quarks in a proton does not obey a simple expression, the emission of the first gluon has the same distribution in transverse space as three dipoles, only with half the intensity. Thus, by modeling the proton with a closed chain of three gluons we emulate the fact that a proton at rest may contain more charges than its valence quarks. This is analogous to the finding of Glück, Reya and Vogt, who needed a large valence-like gluon component when trying to fit parton densities evolved from a very low scale [19]. Thus, although not a fully realistic description of the initial non-perturbative proton state, the model appears to give a fair representation of the multi-dipole system obtained at low x-values, which are important for the high-energy collisions.

The results turned out to be almost independent of the shape of the three starting gluons, except for the size of the triangle. In fact, equilateral triangles that were allowed to vary in only size and orientation turned out to model the proton as well as more complicated formations. With a Gaussian distribution for the size of equilateral triangles, motivated by the exponential dependence on t for the elastic cross section, data on total cross sections for DIS and pp collisions are well reproduced, when the width of the Gaussian was tuned to 3.5 $\mathrm{GeV}^{-1} \approx 0.66$ fm.

As discussed above, the differential and elastic cross sections are determined by the fluctuations in the scattering amplitude, and in [3] it was pointed out that a Gaussian wave function as discussed above must overestimate the fluctuations of the incoming state in its rest frame. The probability for the three quarks to simultaneously be located in a single point ought to be suppressed, and it was emphasized that the exponential t-dependence of the elastic cross section, which motivated the Gaussian shape, is only observed for $|t| < 0.15\,\mathrm{GeV}^2$, corresponding to $b \gtrsim 1$ fm. A wave function of the form

$$|\Psi|^2 = C\mathrm{e}^{-(r-R_p)^2/w^2} \tag{4.1}$$

was also tested, and it was found to give essentially identical total cross sections. The fluctuations are here suppressed by a small value of w, and in [3] it was observed that reducing the fluctuations to a minimum gave good agreement with the integrated elastic and diffractive cross sections in pp collisions. Lacking further constraints we could, however, only present an upper limit for σ_{el}, by neglecting the fluctuations in the wave function, thus including only those in the cascade evolution.

An essential motivation for the present analysis of quasi-elastic $\gamma^* p$ cross sections and of the t-dependence of the pp elastic cross section is to check whether the fluctuations in the dipole cascade model are also consistent with these observables, and if more constraints can be put on the shape of the initial proton state. In this analysis we will use the

two-parameter form in (4.1), and we shall see if this can be adjusted to reproduce also the (quasi-) elastic cross sections.

At this point we also note that in many analyses the fluctuations in the cascade evolution are neglected. This means that e^{-F} is replaced by $e^{-\langle F\rangle}$ in (2.4) and (2.5). Including also the fluctuations in the cascade implies that the impact-parameter profile has to be more "gray" and less "black and white". As an example the amplitude $\langle T(b=0)\rangle$ is a factor 2/3 smaller in our formalism than in the analysis by Kowalski and Teaney [20], for a dipole of size $2\,\mathrm{GeV}^{-1}$ and $x = 10^{-4}$–10^{-5}.

4.2 Photon wave function

4.2.1 Large Q^2

For large Q^2 the coupling of the γ^* to the $q\bar{q}$ pair can be calculated perturbatively. The well-known result to leading order is

$$\begin{aligned}\Psi^{\gamma 0}_{fh\bar{h}}(Q,r,z) &= \frac{\sqrt{\alpha_{\mathrm{EM}}N_C}}{\pi}Qz(1-z)e_f K_0(r\varepsilon_f)\delta_{h\bar{h}},\\ \Psi^{\gamma +}_{fh\bar{h}}(Q,r,z) &= \frac{\sqrt{\alpha_{\mathrm{EM}}N_C/2}}{\pi}e_f\\ &\quad\times\left(\mathrm{i}e^{\mathrm{i}\theta}\left(z\delta_{h+}\delta_{\bar{h}-}-(1-z)\delta_{h-}\delta_{\bar{h}+}\right)\right.\\ &\quad\left.\times\,\varepsilon_f K_1(r\varepsilon_f)+\delta_{h+}\delta_{\bar{h}+}m_f K_0(r\varepsilon_f)\right),\end{aligned} \tag{4.2}$$

with

$$\varepsilon_f = \sqrt{z(1-z)Q^2+m_f^2}. \tag{4.3}$$

Here $\lambda = 0$ and $+$ denote the longitudinal and transverse wave functions, respectively, f denotes the quark flavor, and K_0 and K_1 are modified Bessel functions. e_f is the electric charge of the quark in units of the proton charge and m_f the effective mass of the quark.

4.2.2 Smaller Q^2

For smaller Q^2 the photon has also a hadronic component. In [21] it was shown that also the total $\gamma^\star p$ cross section at HERA could be well described over a wide range of energies and virtualities, when the hadronic component was simulated by a relatively small effective quark mass ≈60 MeV. For the exclusive reactions studied here we need a more careful treatment of the hadronic component, and we expect that these processes can provide relevant constraints on the photon wave function. The hadronic component should be particularly important for the real photons produced in deeply virtual Compton scattering (DVCS).

For small Q^2 a small effective quark mass allows for rather large dipoles with a corresponding large cross section. In the present analysis we include an improved description of confinement effects in the dipole evolution (see Sect. 3.3), and we will therefore try to include confinement effects also in the photon wave function. Our photon model is inspired by the vector meson dominance modeling introduced by Forshaw et al. in [9] (which, in turn, was inspired by [22]). This model contains an enhancement factor for dipoles of a typical hadronic size, together with a large quark mass which suppresses dipoles larger than the confinement scale. In our model we will use the same enhancement factor, but we use a suppression of large dipoles related to the confinement scale $r_{\max}$, instead of the large quark mass used in [9].

The actual implementation in our MC program relies on shrinking dipoles larger than $r_{\max}$ by reducing the size r_{pert} generated according to the perturbative photon wave function to r_{soft}, defined by

$$r_{\mathrm{soft}}(r_{\mathrm{pert}}) = R_{\mathrm{shrink}}\sqrt{\ln\left(1+\frac{r_{\mathrm{pert}}^2}{R_{\mathrm{shrink}}^2}\right)}. \tag{4.4}$$

For small dipoles this gives $r_{\mathrm{soft}} \approx r_{\mathrm{pert}}$, but for large dipoles it gives a Gaussian suppression. The parameter R_{shrink} is adjusted to give the same effective cutoff, $r_{\max}$, as the one obtained for large dipoles in the cascade evolution. This is obtained for $R_{\mathrm{shrink}} = 4.3\ \mathrm{GeV}^{-1}$.

The enhancement factor for dipoles with a typical hadronic size, introduced in [9], is given by the formula

$$f(r) = \frac{1+B_V\exp(-(r-R_V)^2/w_V^2)}{1+B_V\exp(-R_V^2/w_V^2)}. \tag{4.5}$$

This factor multiplies the squared photon wave function after the shift in (4.4). The enhancement resembles very much the shape we use for the proton wave function in (4.1), and we can think of the whole correction

$$\left|\Psi_\gamma(r_{\mathrm{pert}})\right|^2 \to \left|\Psi_\gamma(r_{\mathrm{soft}})\right|^2 f(r_{\mathrm{soft}}) \tag{4.6}$$

as the modeling of the virtual photon fluctuating into vector meson states with r-values of a hadronic scale. Partly this enhancement can be thought of as due to a longer lifetime of these states, and partly a simulation of a gluonic component in the vector meson, in a way similar to our model of the initial proton wave function in Sect. 4.1. The photon model contains three adjustable parameters, B_V, R_V, and w_V, which have to be determined from experiment.

4.3 Meson wave functions

The wave function of a vector meson cannot be calculated perturbatively and has to be described by models. In the rest

frame it is generally assumed that the lowest Fock state with a single $q\bar{q}$ pair dominates. This component must then be normalized to 1, in contrast to the photon for which the $q\bar{q}$ state is a perturbative fluctuation. In addition, the wave function at the origin is determined by the decay rate of the vector meson. Thus there are two constraints allowing two parameters in an ansatz to be determined. In a boosted frame higher Fock states may then be generated by gluon emission. Different models can differ in the functional form used for the wave function in the rest frame, and in the description of the transition from coordinate space to the momentum fractions z and $1-z$ used in the light-cone wave function. We will here concentrate on the DGKP model [23] and the boosted Gaussian model [9], which in the analysis by Forshaw et al. give the best agreement with the experimental data.

In both models, the wave function in momentum light-cone coordinates is assumed to have the same spin structure as the photon wave function, and the relative scalar factor is parameterized by a function $\Gamma_\lambda(k,z)$, such that

$$\Psi^{V\lambda}_{h\bar{h}}(k,z) = \sqrt{\frac{N_c}{4\pi}}\frac{\bar{u}_h(\mathbf{k})}{\sqrt{z}}\big(\gamma,\varepsilon^\lambda_V\big)\frac{v_{\bar{h}}(-\mathbf{k})}{\sqrt{1-z}} \times \frac{z(1-z)\Gamma_\lambda(k,z)}{-z(1-z)M_V^2+k^2+m_f^2}. \tag{4.7}$$

If the polarization vectors are written out explicitly, the longitudinal meson wave function is proportional to

$$\frac{z(1-z)2M_V\Gamma_\lambda(k,z)}{-z(1-z)M_V^2+k^2+m_f^2}+\frac{\Gamma_\lambda(k,z)}{M_V}. \tag{4.8}$$

In the case of a photon the second term corresponds to a term equal to $-1/Q$. This represents a dipole of vanishing size and would not contribute to the cross section. The dependence on $\mathbf{k}$ in the meson case implies that also the second term contributes, which creates problems with gauge invariance. Apart from choosing different functions $\Gamma_\lambda(k,z)$, the two models also differ in that DGKP neglects this second term, while this term is kept in the boosted Gaussian model. This is represented by a parameter δ, taking the values 0 (DGKP) or 1 (boosted Gaussian). More details can be found in [9] and references therein.

4.3.1 The DGKP model

In this model for the meson wave function, proposed by Dosch, Gousset, Kulzinger, and Pirner [23], it is assumed that the dependence on the transverse and longitudinal coordinates, r and z, factorizes. The transverse part of the wave function is assumed to be a pure Gaussian, consistent with soft hadron–hadron collisions. For the longitudinal component it assumes the form proposed by Wirbel, Stech and Bauer [24]. The resulting light-cone wave function has the following form:

$$\begin{aligned}\Psi^{V0}_{f h\bar{h}}(r,z) &= \mathcal{N}_0 M_V \delta_{-h\bar{h}} z(1-z)\sqrt{z(1-z)} \\ &\quad\times\exp\left(-\frac{r^2\omega_L^2}{2}\right)\exp\left(-\frac{M_V^2(z-0.5)^2}{2\omega_L^2}\right),\\ \Psi^{V+}_{f h\bar{h}}(r,z) &= \mathcal{N}_+\sqrt{z(1-z)}\big(\omega_T^2 r\mathrm{i}\mathrm{e}^{\mathrm{i}\theta}(z\delta_{h+}\delta_{\bar{h}-} \\ &\quad-(1-z)\delta_{h-}\delta_{\bar{h}+})+m_f\big) \\ &\quad\times\exp\left(-\frac{M_V^2(z-0.5)^2}{2\omega_T^2}\right)\exp\left(-\frac{r^2\omega_T^2}{2}\right).\end{aligned} \tag{4.9}$$

Here M_V is the mass of the vector meson, and the size parameter ω and the normalization constant $\mathcal{N}$ are determined from the electronic decay rate and the normalization condition. (Our notation differs from the original paper, as we have collected the multiplicative factors in the normalization constant $\mathcal{N}$.) The shape of the wave function of the ρ with the parameters we have used (see Table 4.1) can be seen in Fig. 4.1.

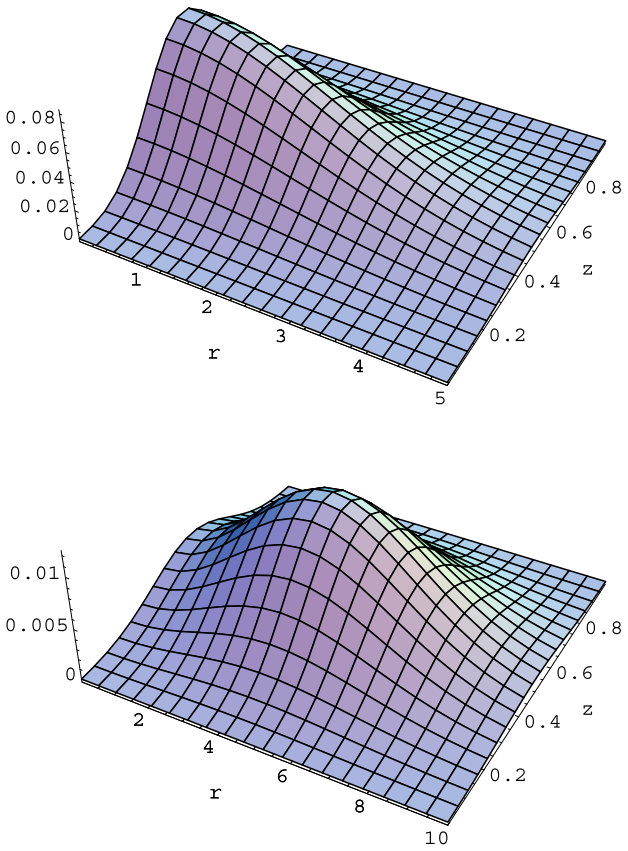

Fig. 4.1 The wave functions $|\Psi_L(r,z)|^2$ (*top*) and $|\Psi_T(r,z)|^2$ (*bottom*) of the DGKP model for a ρ meson with our quark mass of 60 MeV. Note the different scales in r, both in GeV^{-1}

Table 4.1 The parameters used for the boosted Gaussian and DGKP wave functions in this paper in GeV-based units

Boosted Gaussian

V	M_V	m_f	R^2	$\mathcal{N}_0$	$\mathcal{N}_+$
ρ	0.77	0.06	12.3	0.44	0.68
ϕ	1.02	0.15	10	0.41	0.63
ψ	3.1	1.4	5.95	0.23	0.32

DGKP

V	M_V	m_f	ω_L	ω_T	$\mathcal{N}_0$	$\mathcal{N}_+$
ρ	0.77	0.06	0.33	0.22	1.63	2.18
ϕ	1.02	0.15	0.37	0.26	1.86	1.91
ψ	3.1	1.4	0.69	0.56	1.28	0.79

4.3.2 *The boosted Gaussian model*

The "boosted" models are obtained by assuming a given wave function in the meson rest frame. This is then boosted into a light-cone wave function using the Brodsky–Huang–Lepage prescription [25], in which the invariant mass of the quark–antiquark pair is the same in the rest frame and the light-cone frames. The result of this procedure is not factorizing in r and z. In the simplest version the initial wave function in the rest frame is a simple Gaussian. In an alternative version by Nemchik et al. [26] a hard Coulomb contribution is added, dominating for small r. For the pure Gaussian version suggested by Forshaw et al., which we assume in this analysis, the resulting wave function has the following form:

$$\begin{aligned}\Psi^{V0}_{f\bar{h}h}(r,z) = {}& \frac{\mathcal{N}_0}{M_V}\exp\left(-\frac{m_f^2R^2}{8z(1-z)}\right)\\ &\times\exp\left(-2z(1-z)\frac{r^2}{R^2}\right)\exp\left(\frac{R^2}{2}m_f^2\right)\\ &\times\left(z(1-z)M_V^2+m_f^2+8\frac{z(1-z)}{R^2}\right.\\ &\left.-\left(4\frac{z(1-z)r}{R^2}\right)^2\right)\delta_{h\bar{h}},\end{aligned}\tag{4.10}$$

$$\begin{aligned}\Psi^{V+}_{f\bar{h}h}(r,z) = {}& \mathcal{N}_+\exp\left(-\frac{m_f^2R^2}{8z(1-z)}\right)\\ &\times\exp\left(-2z(1-z)\frac{r^2}{R^2}\right)\exp\left(\frac{R^2}{2}m_f^2\right)\\ &\times\left(4z(1-z)\frac{r}{R^2}\mathrm{i}e^{\mathrm{i}\theta}\left(z\delta_{h+}\delta_{\bar{h}-}\right.\right.\\ &\left.\left.-(1-z)\delta_{h-}\delta_{\bar{h}+}\right)+m_f\delta_{h+}\delta_{\bar{h}+}\right).\end{aligned}\tag{4.11}$$

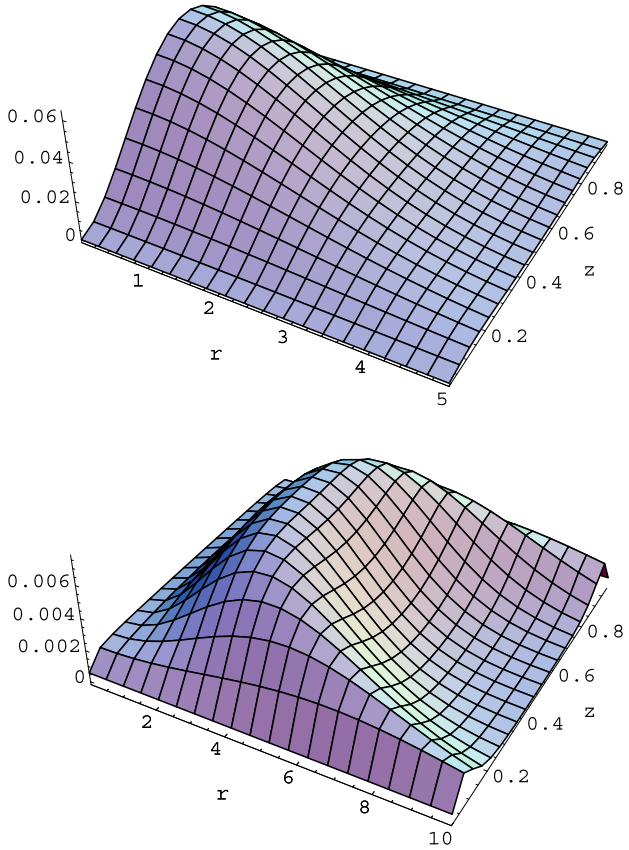

Fig. 4.2 The wave functions $|\Psi_L(r,z)|^2$ (*top*) and $|\Psi_T(r,z)|^2$ (*bottom*) of the boosted Gaussian model for a ρ meson with our quark mass of 60 MeV. Note the different scales in r, both in GeV^{-1}

In this model the transverse size R of the meson and the normalization $\mathcal{N}_\lambda$ are the two parameters to be determined from the normalization and decay width. (In our notation all multiplicative constants have also here been included in a single normalization constant.) The shape of the wave function for the ρ meson using the parameters in Table 4.1 is shown in Fig. 4.2.

5 Tuning of parameters and the differential *pp* cross section

5.1 The total and elastic *pp* cross section

We start by tuning the model to pp scattering data. Here the model contains four parameters, Λ_{QCD} and $r_{\max}$ describing the dipole evolution, and R_p and w determining the proton wave function in (4.1) (with C fixed by normalization). In [3] we found that the values for Λ_{QCD} and $r_{\max}$ are correlated, such that a larger $r_{\max}$ can be compensated by a smaller Λ_{QCD}. It was also noted that the integrated elastic cross section favors a narrow proton wave function, corresponding to a small value for the parameter w. A large w-value, or a single Gaussian $\propto\exp(-\mathbf{r}^2/R_p^2)$, gives too large

fluctuations and correspondingly a too small elastic cross section. To constrain the fit we here add the differential cross section $\mathrm{d}\sigma/\mathrm{d}t$ to the integrated cross sections σ_{tot}, σ_{diff}, and σ_{el} studied in [3]. We will then in the next section check if the result also can reproduce the quasi-elastic cross sections in $\gamma^* p$ collisions.

With the proton wave function given by (4.1) the total and elastic cross sections are given by

$$\sigma_{\mathrm{tot}} = 2\int \mathrm{d}^2\mathbf{b} \times \int \mathrm{d}^2\mathbf{r}_{p1}\,\mathrm{d}^2\mathbf{r}_{p2}\left|\Psi_p(\mathbf{r}_{p1})\right|^2\left|\Psi_p(\mathbf{r}_{p2})\right|^2 \times \left\langle 1-\mathrm{e}^{-F}\right\rangle_{12}, \tag{5.1}$$

$$\sigma_{\mathrm{el}} = \int \mathrm{d}^2\mathbf{b} \times \left|\int \mathrm{d}^2\mathbf{r}_{p1}\,\mathrm{d}^2\mathbf{r}_{p2}\left|\Psi_p(\mathbf{r}_{p1})\right|^2\left|\Psi_p(\mathbf{r}_{p2})\right|^2 \times \left\langle 1-\mathrm{e}^{-F}\right\rangle_{12}\right|^2. \tag{5.2}$$

Here $\mathbf{b}$ is the impact parameter; $\mathbf{r}_{pi}$ $(i=1,2)$ parameterizes the size and orientation of the triangles describing the colliding protons. The Monte Carlo routine is used to simulate the dipole evolution in the rest frame of the collision and to calculate $1-\mathrm{e}^{-F}$. The average $\langle 1-\mathrm{e}^{-F}\rangle_{12}$ is over simulations for fixed impact parameter and starting dipole states $\mathbf{r}_1$ and $\mathbf{r}_2$. Note that in the elastic cross section the average over evolutions and the integrals over the wave functions are taken on amplitude level before taking the absolute square.

When tuning the parameters we find that all observables are almost independent of w below 0.5 GeV^{-1}. We therefore decided to neglect the fluctuations in the proton size completely and set the width to zero, turning the proton wave function into a delta function at R_p.

If the total and integrated elastic cross sections are tuned at one energy, we find that the energy dependence of these cross sections depends very weakly, if at all, on the parameters of the model. Thus this energy dependence cannot be tuned, and the fact that it is close to the experimental results is therefore a direct consequence of the model. Our results for the total and elastic pp cross sections can be seen in Fig. 5.1.

Extrapolating to higher energies we find the total cross section at the LHC nominal energy, 14 TeV, to be about 125 mb (117 mb at 10 TeV). We note that this is a rather high value compared to other predictions. Thus the Donnachie–Landshoff parameterization gives 101.5 mb at 14 TeV [33], while an analysis by Khoze, Martin, and Ryskin gives about 90 mb [34]. The predicted elastic cross section is about 31 mb for the LHC at 14 TeV (28 mb at 10 TeV).

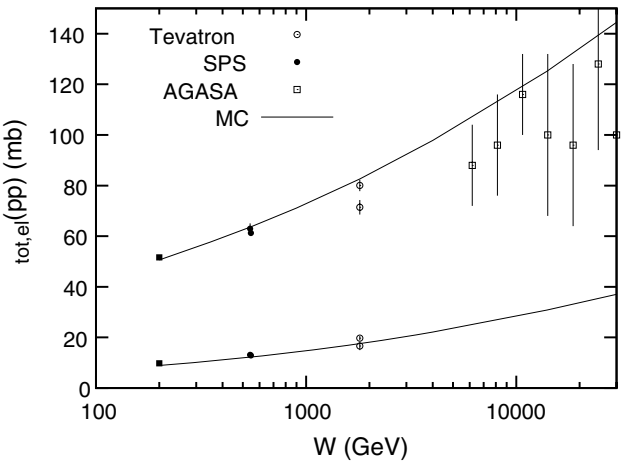

Fig. 5.1 The total and elastic cross section for pp collisions. The upper cross sections are total cross sections, while the lower cross sections are the elastic ones. Tevatron data are from [27–30], SPS data are from [31] and cosmic-ray data are from [32]. The lines are our model with tuned parameters

5.2 The differential elastic pp cross section

The differential elastic pp cross section is given by

$$\frac{\mathrm{d}\sigma_{\mathrm{el}}}{\mathrm{d}t} = \frac{1}{4\pi}\left|\int \mathrm{d}^2\mathbf{b}\mathrm{e}^{-\mathrm{i}\mathbf{q}\cdot\mathbf{b}}\,\mathrm{d}^2\mathbf{r}_{p1}\mathrm{d}^2\mathbf{r}_{p2} \times \left|\Psi_p(\mathbf{r}_{p1})\right|^2\left|\Psi_p(\mathbf{r}_{p2})\right|^2\left\langle 1-\mathrm{e}^{-F}\right\rangle_{12}\right|^2. \tag{5.3}$$

We here neglect the real part of the amplitude, and therefore $\mathrm{d}\sigma/\mathrm{d}t$ will have zeroes from the Fourier transform of the amplitude in (5.3). Even though the true complex amplitude will not be identically zero, the real part is still assumed to be small, producing a dip at some value $t=t_0$, related to the inverse square of the size of the proton at the relevant energy. This dip is visible in some of the experimental data shown in Fig. 5.2, where we have also included the results from the simulations. The parameters which are most sensitive to these distributions are R_p, which determines the size of the proton at rest, and r_{max}, which regulates the maximal size of new dipoles, and therefore the increase with energy of the proton radius and the variation of the dip position. However, the slope of the distribution is basically independent of our parameters, as is the cross section at large t-values. Nevertheless, we are able to get a very good description of the data at all t-values even though the cross sections vary over many orders of magnitude. In Fig. 5.2 we also show our result for the LHC, which predicts the location of the dip in the t-dependence at 0.43 GeV^2 at $\sqrt{s}=14$ TeV (0.47 GeV^2 at 10 TeV). The values of the tuned parameters can be found in Table 5.1.

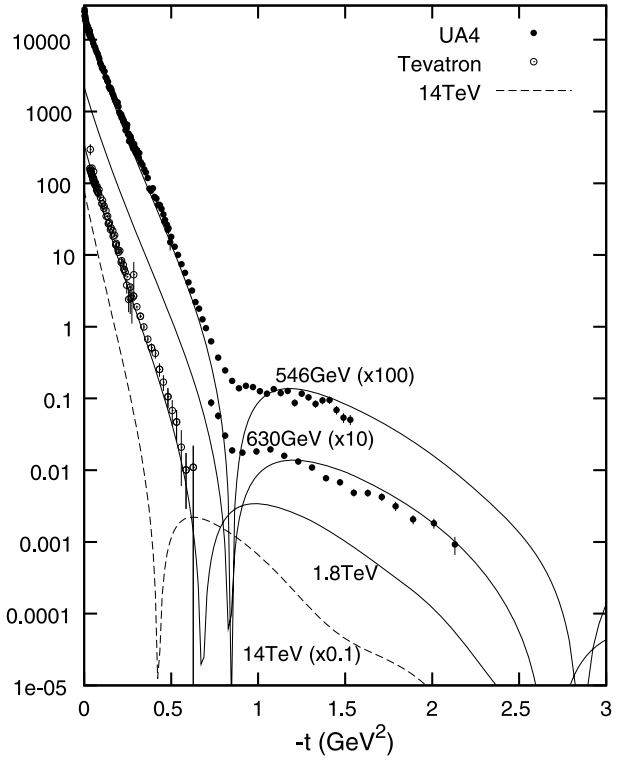

Fig. 5.2 The elastic cross section as function of t in mb/GeV^2. The numbers in parentheses indicate how the data have been scaled. The *lines* are our model with tuned parameters. Predictions for 14 TeV are also included. Data are from [27, 35, 36] and [37]

Table 5.1 The tuned values the parameters for the proton wave function and the perturbative evolution used for our model throughout this paper

$\Lambda_{\rm QCD}$	0.2 GeV
$r_{\max}$	2.9 GeV^{-1}
R_p	3.0 GeV^{-1}
w	0 GeV^{-1}

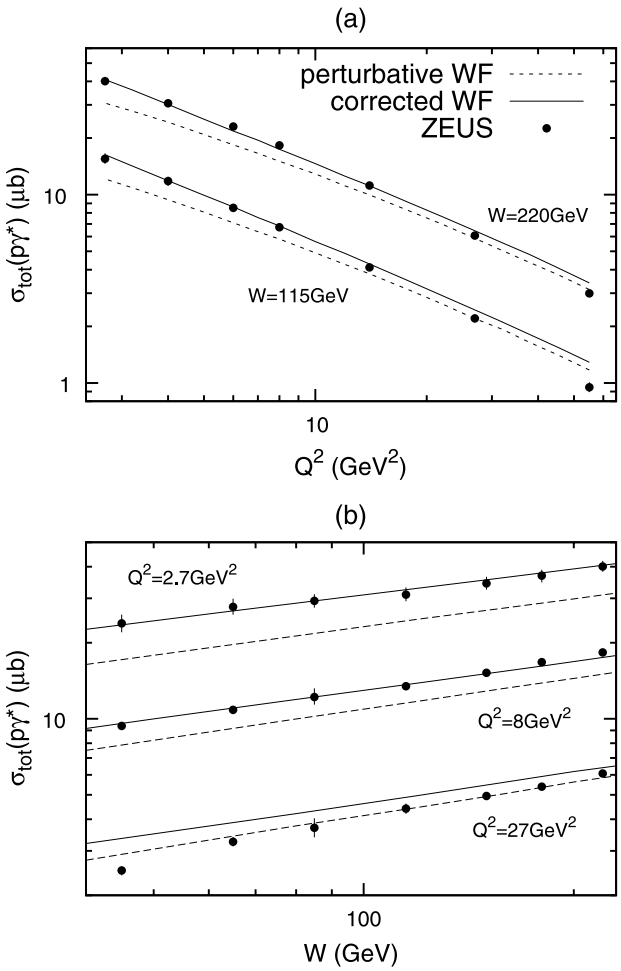

Fig. 5.3 The total cross section of photon–proton collisions as a function of photon virtuality and center-of-mass energy. The *dashed line* is calculated with a purely perturbative photon wave function, while the *full line* is with a photon wave function with both confinement and VMD corrections. Experimental data are from [39]

5.3 The total $\gamma^\star p$ cross section and tuning the photon wave function

We shall here use $\Psi_\gamma(Q, \mathbf{r}, z)$ to denote the photon wave function in (4.6), where for small Q^2 the perturbative wave function is modified to account for the hadronic component of the photon. The total $\gamma^* p$ cross section can be written

$$\sigma_{\rm tot}(\gamma^* p) = \sum_{\lambda f} \int \mathrm{d}^2\mathbf{b}\,\mathrm{d}^2\mathbf{r}_p\,\mathrm{d}^2\mathbf{r}\,\mathrm{d}z \times \left|\Psi_p(\mathbf{r}_p)\right|^2 \left|\Psi^\lambda_{\gamma,f}(Q,\mathbf{r},z)\right|^2 \left\langle 1-\mathrm{e}^{-F}\right\rangle_{\rm dp}, \tag{5.4}$$

where λ is the polarization of the photon and f is the flavor of the quark–antiquark pair created by the photon. $\langle 1-\mathrm{e}^{-F}\rangle_{\rm dp}$ is now an average of the evolution of the dipole from the photon side and of the dipoles from the proton side. It depends not only on the total energy, the size of the proton and photon dipoles and b, but it also has a weak dependence on z.

The three parameters B_V, R_V and w_V in the enhancement factor in (4.5) were fitted to the total $\gamma^\star p$ cross section as measured at HERA. Here the value of R_V determines the range in Q^2 where the enhancement is significant, while w_V determines how fast it falls off for large Q^2. The parameter B_V is just an overall strength of the hadronic component.

A good fit to the data was obtained with a wave function for the hadronic component similar to the proton wave function, having a size $R_V \approx 3$ GeV^{-1} and a small width. The total $\gamma^\star p$ cross section with and without the effects of confinement and vector meson contributions are shown in Fig. 5.3. The tuned values are given in Table 5.2. These parameters are quite different from the ones used by Forshaw et al., who had an R_V of 6.84 GeV^{-1} and a fairly large width [38], which thus gives a stronger enhancement for large dipoles. For large dipole sizes the elementary dipole–

Table 5.2 The tuned values of the parameters of the vector meson resonance function $f(r)$ used for our model throughout this paper

R_V	$3.0\,\mathrm{GeV}^{-1}$
w_V	$0.2\,\mathrm{GeV}^{-1}$
B_V	9.0

proton cross sections assumed in [9] are also significantly different from the corresponding ones in our model. The reason why we anyhow can get similar results is that in [9] the very large dipoles are suppressed by a large quark mass, and the enhancement is therefore not very effective. A reason for a smaller width in our wave function is also that fluctuations in the dipole cascade are included in our formalism, which is compensated by less fluctuations in the wave function.

We also note that the cross sections presented in Fig. 5.3 are somewhat smaller than the corresponding results in [3] and [21]. This is a consequence of the more consistent treatment of confinement in the present analysis, which gives a stronger suppression for larger dipoles. We believe, however, that a much stronger test of the hadronic component will rely on the results for the quasi-elastic reactions discussed in next section.

6 Results for quasi-elastic $\gamma^\star p$ collisions

In this section we shall study predictions for quasi-elastic $\gamma^* p$ collisions, using the photon wave function parameters determined in Sect. 5.3.

6.1 Deeply virtual Compton scattering

In deeply virtual Compton scattering, DVCS, the incoming particle is a virtual photon, while the outgoing particle is a real photon with wave function $\Psi^{\lambda}_{\gamma,f}(0,\mathbf{r},z)$. According to (2.7) and (2.8) the cross section is given by

$$\sigma_{\mathrm{DVCS}} = \int \mathrm{d}^2\mathbf{b} \sum_{\lambda} \left| \int \mathrm{d}^2\mathbf{r}_p\, \mathrm{d}^2\mathbf{r}\, \mathrm{d}z \sum_f \left|\Psi_p(\mathbf{r}_p)\right|^2 \times \Psi^{\star\gamma\lambda}_f(Q,\mathbf{r},z)\Psi^{\gamma\lambda}_f(0,\mathbf{r},z)\left\langle 1-\mathrm{e}^{-F}\right\rangle_{\mathrm{dp}} \right|^2. \quad (6.1)$$

The results obtained using the parameter values in Table 5.2 are presented in Fig. 6.1. We see that the results from the model indeed agree with the data, both in normalization and in the dependence on Q^2 and W. As this quasi-elastic reaction is very sensitive to the fluctuations and the transverse size of the hadronic component of the real photon, this is qualitative support for the proton-like wave function.

The differential cross section $\mathrm{d}\sigma/\mathrm{d}t$ is obtained from the Fourier transform as shown in (2.10). The result is presented

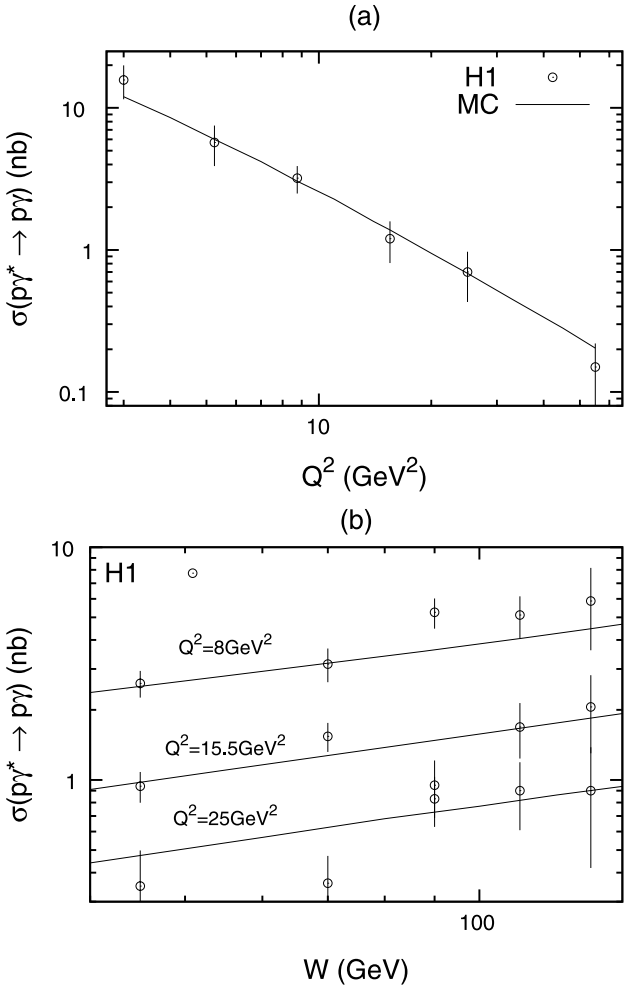

Fig. 6.1 The cross section of $\gamma^\star p \to \gamma p$ for $W = 82$ GeV as a function of Q^2 (**a**) and as a function of W for three different Q^2 (**b**). Experimental data are from [40, 41]

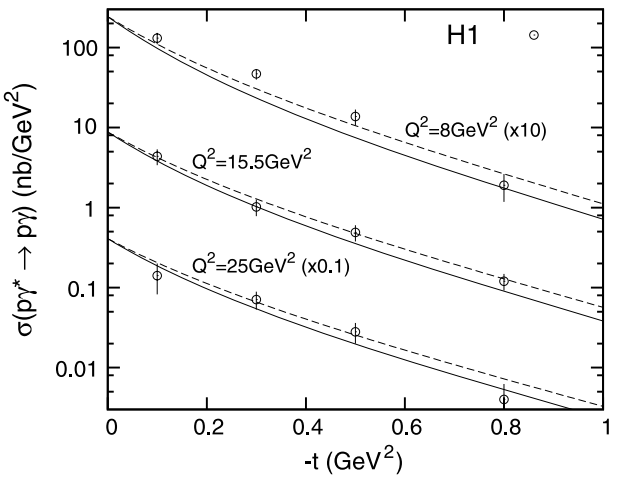

Fig. 6.2 The cross section of $\gamma^\star p \to \gamma p$ as a function of t at $W = 82$ GeV. *Dashed lines* are without the effects of scewedness (see Sect. 2.3), while the *full lines* are from the complete model. Note that the three series have been scaled by 10, 1, and 0.1 for better readability. Experimental data are from [41]

in Fig. 6.2, which also shows the result obtained if the effects of scewedness are not included. We see that these effects increase the slope by about 7% at $Q^2 = 8$ GeV^2 and 4% at $Q^2 = 25$ GeV^2. The agreement with the data is quite good, both with and without scewedness effects. It is actually somewhat better without them, but we think that the difference is smaller than the uncertainty from the hadronic part of the photon wave function.

6.2 Exclusive production of light vector mesons

The cross section for exclusive vector meson production, $\gamma^\star p \to Vp$, can be calculated in exactly the same way as for DVCS, only replacing the real photon wave function by a meson wave function:

$$\sigma_{\mathrm{el}} = \int \mathrm{d}^2\mathbf{b} \sum_\lambda \left| \int \mathrm{d}^2\mathbf{r}\, \mathrm{d}^2\mathbf{r}_p\, \mathrm{d}z \sum_f \left|\Psi_p(\mathbf{r}_p)\right|^2 \right.$$
$$\left. \times\, \Psi_f^{\star\gamma\lambda}\big(Q^2, \mathbf{r}, z\big)\Psi_f^{V\lambda}(\mathbf{r}, z)\big\langle 1 - \mathrm{e}^{-F}\big\rangle_{\mathrm{dp}} \right|^2. \qquad (6.2)$$

As before we have ignored the real part of the amplitude. Contrary to the case of pp scattering it has been shown in [9] that in exclusive production of light vector mesons the real part can be quite large, for large Q^2 or large W as large as one half of the imaginary part. This would mean that we underestimate the cross section by up to 25% in these regions. However, compared to the uncertainties in the vector meson wave functions, this error is small.

From our tuning of the hadronic part of the photon wave function, it could seem natural to assume some universal hadron size and maybe try to model the vector meson wave functions as a simple gluon–gluon dipole with a size of 3 GeV^{-1} and a small width. However, this would not naturally give us a z-dependence and we would not include the possibility that the vector meson may fluctuate into a photon, which could correspond to an enhancement at small r-values. Therefore, we will simply use the boosted Gaussian and DGKP wave functions introduced in Sect. 4.3 to estimate the $\gamma^\star p \to Vp$ cross section. Throughout we will use the parameters listed in Table 4.1.

As before, the t-dependence of the cross section can be calculated through a Fourier transform of the amplitude. We are also able to calculate the ratio between the longitudinal and the transverse cross sections and compare them with the experimental data.

Starting with ρ meson production, the results are shown in Figs. 6.3 and 6.4. We see that the model calculations reproduce the experimental data rather well, including the dependence on virtuality Q^2, energy W and momentum transfer t. The t-dependence includes effects of scewedness (which are of the same size as for the DVCS case in Fig. 6.2) and it is a bit too steep, especially for small Q^2. The boosted

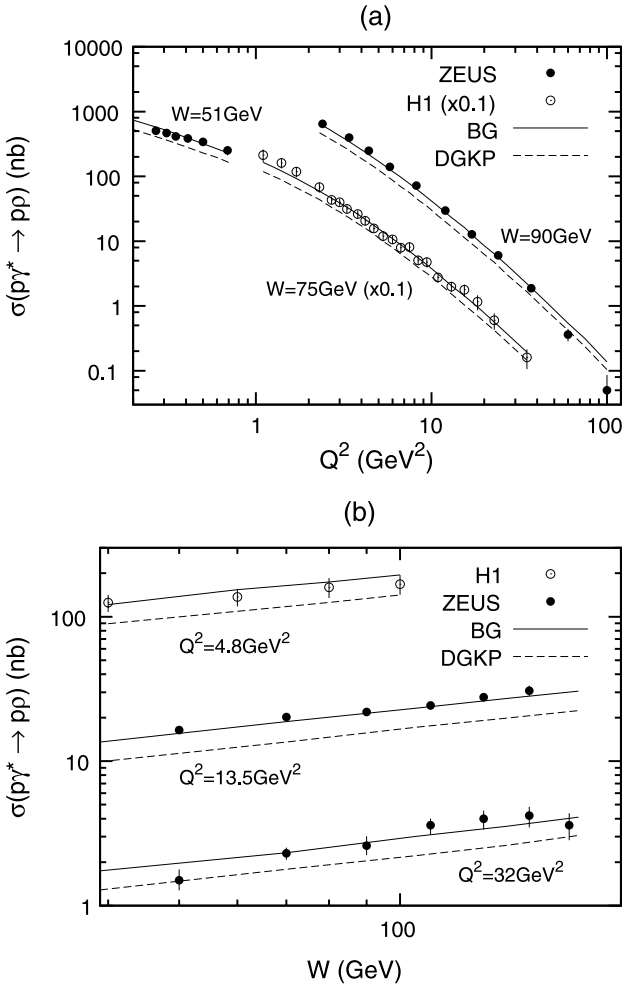

Fig. 6.3 The cross section for $\gamma^\star p \to \rho p$, (**a**) as a function of the photon virtuality. The H1 data have been moved down a factor 10 for better readability. The *full* and *dashed lines* are with the two different meson wave function described in Sect. 4.3. (**b**) The same as a function of the center-of-mass energy W. Experimental data are from [42–44]

Gaussian wave function is in general providing the closer fit, while DGKP is having problems mainly in the ratio between longitudinal and transverse cross sections. It should be noted, however, that this ratio could be changed if we decided to use different parameters for the resonance function in (4.5) for the different polarizations.

Also in ϕ production our model agrees well with the experimental data, as can be seen in Figs. 6.5 and 6.6. The qualitative properties are similar to those of ρ production.

We note that the more stringent test of the hadronic component of the photon is obtained from DVCS. The ratio between vector meson production and DVCS is then more a test of the vector meson wave functions. It is therefore not surprising that we here get results similar to those in [9]. The t-dependence presented in Fig. 6.4 is, however, a result which in our model is sensitive to both the photon and vector meson wave functions, while in [9] it was fixed by the

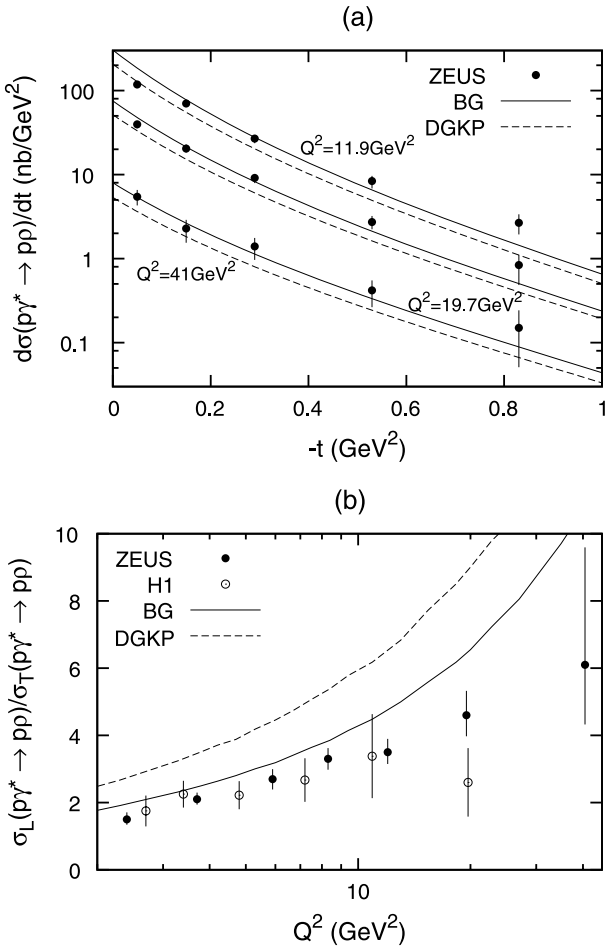

Fig. 6.4 (**a**) The differential cross section for $\gamma^\star p \to \rho p$ as a function of the transferred momentum squared $|t|$. Three different Q^2 have been used, all with a center-of-mass energy of 90 GeV. (**b**) The ratio of longitudinal and transverse cross section for $\gamma^\star p \to \rho p$ as a function of the photon virtuality. Experimental data are from [42, 43]

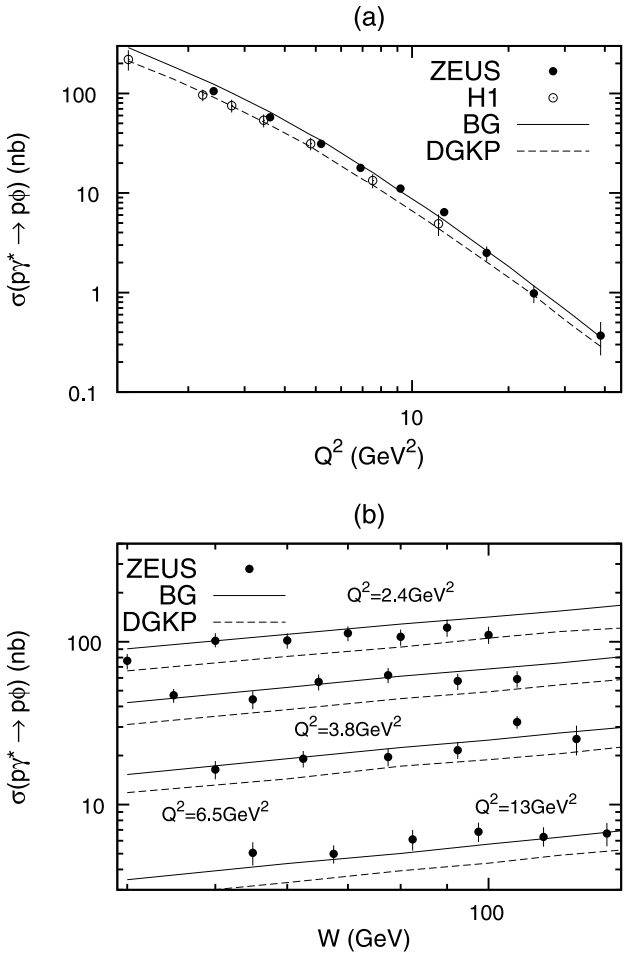

Fig. 6.5 The cross section for $\gamma^\star p \to \phi p$ (**a**) as a function of the photon virtuality at center-of-mass energy 75 GeV. The *full* and *dashed lines* are with the two different meson wave function described in Sect. 4.3. (**b**) The same as a function of the center-of-mass energy for four different photon virtualities Q^2. Experimental data are from [45, 46]

experimental data. From Fig. 6.4 we see that for lower Q^2 the slope in the model is somewhat too steep, thus indicating a too wide wave function for the ρ meson. We see from Figs. 4.1 and 4.2 that the ρ wave functions for transverse polarization are extending well beyond 5 GeV^{-1}. A faster falloff for large r-values would here give a better agreement with the observed t-dependence.

6.3 Exclusive ψ production

In the case of ψ production we necessarily encounter more uncertainties. The result is sensitive to the mass of the charm quark, and here we use the value 1.4 GeV, which in the analysis in [21] gave the correct charm contribution, F_2^c, to the proton structure function. We have not included a ψ component in the photon wave function, although this would in principle be possible. For the ψ meson wave function we use the parameters in Table 4.1.

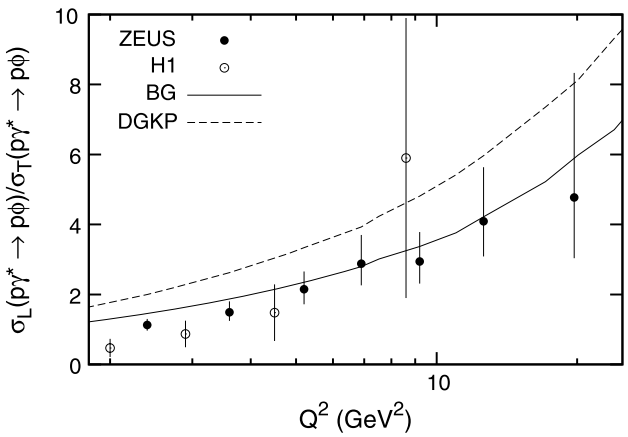

Fig. 6.6 The ratio of longitudinal and transverse cross section for $\gamma^\star p \to \phi p$ as a function of the photon virtuality at a center-of-mass energy of 75 GeV. Experimental data are from [45, 46]

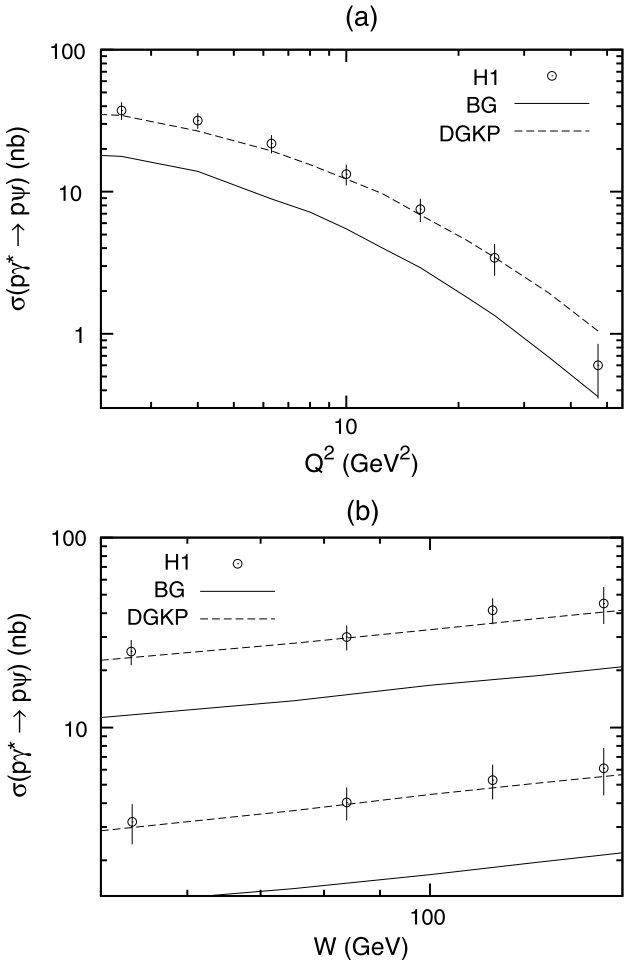

Fig. 6.7 The cross section for $\gamma^\star p \to \psi p$ (**a**) as a function of the photon virtuality at center-of-mass energy 90 GeV. The *full* and *dashed lines* are with the two different meson wave function described in Sect. 4.3. (**b**) The same as a function of center-of-mass energy for $Q^2 = 22.4\ \mathrm{GeV}^2$ (*lower data*) and $3.2\ \mathrm{GeV}^2$ (*upper data*). Experimental data are from [47]

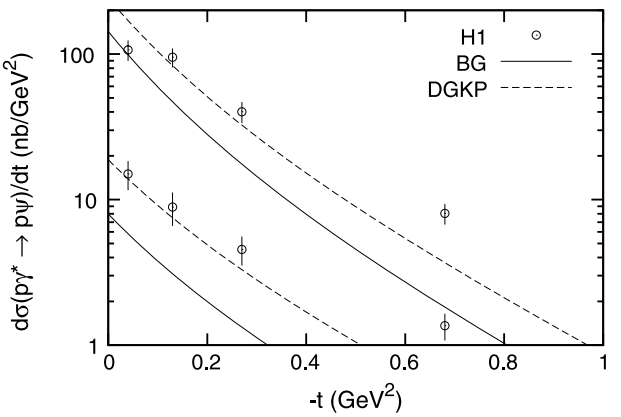

Fig. 6.8 The cross section for $\gamma^\star p \to \psi p$ as a function of transferred momentum squared t for $Q^2 = 22.4\ \mathrm{GeV}^2$ (*lower data*) and $3.2\ \mathrm{GeV}^2$ (*upper data*). Experimental data are from [47]

Our results are presented in Figs. 6.7 (dependence on Q^2 and W) and 6.8 (dependence on t). We note that, in contrast to the results for the lighter mesons, the boosted Gaussian wave function here gives a too low cross section over the entire kinematic region, while the DGKP model agrees very well both in its normalization and in its dependence on Q^2 and W. This result is a consequence of the stronger emphasis on small dipoles in the case of the ψ. Both models show, however, a somewhat steeper t-dependence than the experimental data. Again we find that this steepness is increased by including scewedness effects described in Sect. 2.3 by approximately the same amount as for the DVCS case in Fig. 6.2. Compared to the corresponding result for ρ meson production, we conclude that also for the ψ meson the parameters in Table 4.1 give somewhat too wide wave functions.

7 Conclusions and outlook

In this paper we have spent some effort on the modeling of non-perturbative aspects of the proton, photon and vector meson wave functions. None of our models are in any way unique or on solid theoretical grounds. However, they do allow us to compare our dipole evolution model directly to the experimental data. Fixing the wave function parameters at one energy we find that the energy dependence of both total and (quasi-) elastic cross sections are well described by the cascade evolution, and this is rather independent of our modeling of the wave functions. Also the slope in $\mathrm{d}\sigma/\mathrm{d}t$ for elastic pp scattering and DVCS is in reasonable agreement with the experimental data independently of the tuning. This indicates a very high predictive power of our evolution model both when it comes to the average multiplicity and sizes of the dipoles (mainly influencing the total cross sections), the rate of increasing transverse size due to the dipole cascade (determining the energy variation in the position of the dip), and the fluctuations (mainly influencing the magnitude of elastic cross sections and their t-dependence).

Nevertheless, our modeling of the non-perturbative wave functions does give us valuable insights. Including the fluctuations in the cascade, the fluctuations in the proton wave function have to be rather small, in order to give the observed elastic cross section. The photon wave function clearly needs a hadronic component with a wave function with similar size as the proton and with similarly small fluctuations. The fact that the size turns out to be the same as the size of our proton may be a coincidence, but it could also indicate that there is a universal size of hadrons, at least when consisting of light-quark flavors.

For the t-dependence of DVCS and vector meson production, we have included the effects of scewedness as calculated in [12], which gives an increase in the slope of the t-dependence. This effect is about 5% at $Q^2 = 8\ \mathrm{GeV}^2$, and

decreasing for larger Q^2-values. For the proton wave function we give arguments indicating that the effects should be small in pp at collider energies and in DIS at HERA.

For the vector meson wave functions we have tested two different forms, which in the analysis by Forshaw et al. gave the best agreement with data for diffractive vector meson production. For light mesons the best result was obtained by the boosted Gaussian wave functions, while for ψ production the DGKP wave function was favored. In both cases the t-dependence was somewhat too steep, indicating that these wave functions extend out to too large r-values, where in particular the wave functions for transverse polarization are much wider than our wave functions for the proton and the photon.

The robustness of our model for dipole evolution, both for inclusive and exclusive cross sections, increases our confidence that it can also be used to model fully exclusive final states. In future publications we will therefore concentrate on turning our Monte Carlo simulation program into a full-fledged event generator, which would then be able to model multi-particle production at e.g. the LHC, with special emphasis on the underlying event and multiple scatterings.

Acknowledgements We want to thank Emil Avsar for valuable discussions. This work is supported in part by the Marie Curie research training network "MCnet" (contract number MRTN-CT-2006-035606) and by the Swedish Foundation for International Cooperation and Higher Education–STINT, contract number 2006/080. Gösta Gustafson also acknowledges support from the Deutsche Forschungsgemeinschaft.

References

1. E. Avsar, G. Gustafson, L. Lönnblad, J. High Energy Phys. **07**, 062 (2005). hep-ph/0503181
2. E. Avsar, G. Gustafson, L. Lonnblad, J. High Energy Phys. **01**, 012 (2007). hep-ph/0610157
3. E. Avsar, G. Gustafson, L. Lonnblad, J. High Energy Phys. **12**, 012 (2007). arXiv:0709.1368
4. A.H. Mueller, Nucl. Phys. B **415**, 373–385 (1994)
5. A.H. Mueller, B. Patel, Nucl. Phys. B **425**, 471–488 (1994). hep-ph/9403256
6. A.H. Mueller, Nucl. Phys. B **437**, 107–126 (1995). hep-ph/9408245
7. G.P. Salam, Comput. Phys. Commun. **105**, 62–76 (1997). hep-ph/9601220
8. A.H. Mueller, G.P. Salam, Nucl. Phys. B **475**, 293–320 (1996). hep-ph/9605302
9. J.R. Forshaw, R. Sandapen, G. Shaw, Phys. Rev. D **69**, 094013 (2004). hep-ph/0312172
10. J.R. Forshaw, R. Sandapen, G. Shaw, J. High Energy Phys. **11**, 025 (2006). hep-ph/0608161
11. A.I. Shoshi, F.D. Steffen, H.J. Pirner, Nucl. Phys. A **709**, 131–183 (2002). hep-ph/0202012
12. J. Bartels, K.J. Golec-Biernat, K. Peters, Acta Phys. Pol. B **34**, 3051–3068 (2003). hep-ph/0301192
13. T. Sjostrand, S. Mrenna, P. Skands, J. High Energy Phys. **05**, 026 (2006). hep-ph/0603175
14. J. Kwiecinski, A.D. Martin, P.J. Sutton, Z. Phys. C **71**, 585–594 (1996). hep-ph/9602320
15. I. Balitsky, Phys. Rev. D **75**, 014001 (2007). hep-ph/0609105
16. Y.V. Kovchegov, H. Weigert, Nucl. Phys. A **789**, 260–284 (2007). hep-ph/0612071
17. I. Balitsky, G.A. Chirilli, NLO evolution of color dipoles. Acta Phys. Pol. Supp. **1**, 545 (2008)
18. M. Praszalowicz, A. Rostworowski, Acta Phys. Pol. B **29**, 745–753 (1998). hep-ph/9712313
19. M. Glück, E. Reya, A. Vogt, Eur. Phys. J. C **5**, 461–470 (1998). hep-ph/9806404
20. H. Kowalski, D. Teaney, Phys. Rev. D **68**, 114005 (2003). hep-ph/0304189
21. E. Avsar, G. Gustafson, J. High Energy Phys. **04**, 067 (2007). hep-ph/0702087
22. L. Frankfurt, V. Guzey, M. Strikman, Phys. Rev. D **58**, 094039 (1998). hep-ph/9712339
23. H.G. Dosch, T. Gousset, G. Kulzinger, H.J. Pirner, Phys. Rev. D **55**, 2602–2615 (1997). hep-ph/9608203
24. M. Wirbel, B. Stech, M. Bauer, Z. Phys. C **29**, 637 (1985)
25. S.J. Brodsky, T. Huang, G.P. Lepage, in *20th Int. Conf. on High Energy Physics*, Madison, Wisc., 17–23 July 1980
26. J. Nemchik, N.N. Nikolaev, E. Predazzi, B.G. Zakharov, Z. Phys. C **75**, 71–87 (1997). hep-ph/9605231
27. F. Abe et al. (CDF Collaboration), Phys. Rev. D **50**, 5518–5534 (1994)
28. F. Abe et al. (CDF Collaboration), Phys. Rev. D **50**, 5550–5561 (1994)
29. N.A. Amos et al. (E-710 Collaboration), Phys. Lett. B **243**, 158–164 (1990)
30. C. Avila et al. (E-811 Collaboration), Phys. Lett. B **537**, 41–44 (2002)
31. C. Augier et al. (UA4/2 Collaboration), Phys. Lett. B **344**, 451–454 (1995)
32. M.M. Block, F. Halzen, T. Stanev, Phys. Rev. D **62**, 077501 (2000). hep-ph/0004232
33. A. Donnachie, P.V. Landshoff, Phys. Lett. B **296**, 227–232 (1992). hep-ph/9209205
34. M.G. Ryskin, A.D. Martin, V.A. Khoze, Eur. Phys. J. C **54**, 199–217 (2008). arXiv:0710.2494
35. N.A. Amos et al. (E-710 Collaboration), Phys. Lett. B **247**, 127–130 (1990)
36. D. Bernard et al. (UA4 Collaboration), Phys. Lett. B **171**, 142 (1986)
37. M. Adamus et al. (NA22 Collaboration), Phys. Lett. B **186**, 223–226 (1987)
38. J.R. Forshaw, G. Kerley, G. Shaw, Phys. Rev. D **60**, 074012 (1999). hep-ph/9903341
39. S. Chekanov et al. (ZEUS Collaboration), Nucl. Phys. B **713**, 3–80 (2005). hep-ex/0501060
40. A. Aktas et al. (H1 Collaboration), Eur. Phys. J. C **44**, 1–11 (2005). hep-ex/0505061
41. F.D. Aaron et al. (H1 Collaboration), Phys. Lett. B **659**, 796–806 (2008). arXiv:0709.4114
42. C. Adloff et al. (H1 Collaboration), Eur. Phys. J. C **13**, 371–396 (2000). hep-ex/9902019
43. S. Chekanov et al. (ZEUS Collaboration), PMC Phys. A **1**, 6 (2007). arXiv:0708.1478
44. J. Breitweg et al. (ZEUS Collaboration), Eur. Phys. J. C **6**, 603–627 (1999). hep-ex/9808020
45. C. Adloff et al. (H1 Collaboration), Phys. Lett. B **483**, 360–372 (2000). hep-ex/0005010
46. S. Chekanov et al. (ZEUS Collaboration), Nucl. Phys. B **718**, 3–31 (2005). hep-ex/0504010
47. A. Aktas et al. (H1 Collaboration), Eur. Phys. J. C **46**, 585–603 (2006). hep-ex/0510016